Draft version February 8, 2024
Typeset using LaTeX **twocolumn** style in AASTeX631

Experimental study of Alfvén wave reflection from an Alfvén-speed gradient relevant to the solar coronal holes

Sayak Bose [1,2] Jason M. TenBarge [2] Troy Carter [3] Michael Hahn [4] Hantao Ji [1,2] James Juno [1] Daniel Wolf Savin [4] Shreekrishna Tripathi [3] and Stephen Vincena [3]

[1] *Princeton Plasma Physics Laboratory, 100 Stellarator Road, Princeton, NJ 08540 USA*
[2] *Department of Astrophysical Sciences, Princeton University, NJ 08544 USA*
[3] *Department of Physics and Astronomy, University of California, Los Angeles, California 90095, USA*
[4] *Columbia Astrophysics Laboratory, Columbia University, 550 West 120th Street, New York, NY 10027 USA*

ABSTRACT

We report the first experimental detection of a reflected Alfvén wave from an Alfvén-speed gradient under conditions similar to those in coronal holes. The experiments were conducted in the Large Plasma Device at the University of California, Los Angeles. We present the experimentally measured dependence of the coefficient of reflection versus the wave inhomogeneity parameter, i.e., the ratio of the wave length of the incident wave to the length scale of the gradient. Two-fluid simulations using the `Gkeyll` code qualitatively agree with and support the experimental findings. Our experimental results support models of wave heating that rely on wave reflection at low heights from a smooth Alfvén-speed gradient to drive turbulence.

Keywords: The Sun (1693), Plasma physics (2089), Plasma astrophysics (1261), Alfvén waves (23), Solar corona (1483), Solar coronal holes (1484), Solar coronal heating (1989), Fast solar wind (1872)

1. INTRODUCTION

Coronal holes are low density regions of the solar atmosphere with open magnetic field lines that extend into interplanetary space. These regions appear as dark areas resembling holes in ultraviolet and X-ray images. Spectroscopic measurements indicate that coronal holes are at 10^6 K, approximately 200 times hotter than the underlying photosphere (Fludra et al. 1999). Despite several decades of research, the physics behind the heating of coronal holes is not well understood (Cranmer 2009; Cranmer et al. 2015).

Alfvén waves are posited to play a significant role in the heating of coronal holes (Alfvén 1942; McIntosh et al. 2011). Perturbations of the foot points of open magnetic field lines, due to the sloshing of the photospheric plasma, are thought to excite the Alfvén waves (Priest 2014). These waves predominantly travel along the magnetic field lines, transporting from the photosphere to the corona the energy necessary for heating coronal holes (Cranmer 2009).

Recent observations have found Alfvénic waves at the base of coronal holes that satisfy the energy budget needed to heat the plasma in coronal holes (McIntosh et al. 2011). The term "Alfvénic" highlights that in addition to Alfvén waves, transverse kink modes may also be present in coronal holes (Van Doorsselaere et al. 2008; Goossens et al. 2009, 2012). Furthermore, the detection of strong damping of Alfvénic waves at low heights in coronal holes suggests that wave-driven processes may be responsible for heating the plasma (Bemporad & Abbo 2012; Hahn et al. 2012; Hahn & Savin 2013; Hara 2019).

The most promising wave-based model put forward to explain the damping of wave energy in coronal holes involves nonlinear interaction between counter-propagating waves, resulting in the development of turbulence, which leads to an irreversible cascade of wave energy to smaller scales, at which the waves are more easily damped, leading to the heating of the plasma (Moore et al. 1991a,b; Matthaeus et al. 1999; Dmitruk et al. 2001; Oughton et al. 2001; Cranmer et al. 2007;

sbose@princeton.edu

Chandran & Hollweg 2009). Recent observations of counter-propagating Alfvénic waves in coronal holes support the wave-turbulence model (Morton et al. 2015). But, the mechanism responsible for the generation of counter-propagating waves is still unknown. Among the different theories put forward to explain the counter-propagating waves (Musielak et al. 1992; Del Zanna et al. 2001), a number of them invoke partial reflection of outward propagating Alfvén waves at low heights in coronal holes due to an Alfvén-speed inhomogeneity along the ambient magnetic field lines (Moore et al. 1991a; Moore et al. 1992; Musielak et al. 1992; Hahn et al. 2018; Asgari-Targhi et al. 2021; Hahn et al. 2022).

Several experiments have been carried out in the past where Alfvén waves were made to propagate through an Alfvén-speed gradient produced by a magnetic field gradient. However, none of those experiments detected a reflected wave (Stix & Palladino 1958; Swanson et al. 1972; Breun et al. 1987; Yasaka et al. 1988; Roberts et al. 1989; Vincena et al. 2001; Mitchell et al. 2002; Bose et al. 2019). An experiment on Alfvén wave propagation through multiple magnetic field wells reported a possible indirect signature of wave reflection (Zhang et al. 2008), but the geometry studied is not relevant to coronal holes.

Here, we report the first direct detection of a reflected Alfvén wave in the laboratory under conditions relevant to coronal holes. The wave experiments were performed in the Large Plasma Device (LAPD; Gekelman et al. (2016); Bose et al. (2019)).

The rest of this paper is organized as follows. A comparison of coronal hole and LAPD parameters relevant to Alfvén wave physics is described in Section 2. The wave experiments and simulations are presented and analyzed in Sections 3 and 4, respectively. In Section 5, we discuss the implication of our results in the solar context. This is followed by a summary in Section 6.

2. ALFVÉN WAVES IN CORONAL HOLES AND LAPD

The plasma and Alfvén wave parameters in LAPD were scaled to match those in coronal holes, to within laboratory limitations, by adpoting the frame work discussed by Bose et al. (2019). In the Sun, Alfvén waves excited in the photosphere (Narain & Ulmschneider 1996; Priest 2014) propagate upward through coronal holes along the ambient magnetic field lines, which are nearly straight. The geometry of LAPD is similar to coronal holes. LAPD is a cylindrical machine, wherein we excite waves at one end of the machine, and the waves follow the magnetic field along the length of the machine.

Table 1. Dimensionless parameters for coronal holes and LAPD

Parameter	Coronal hole	LAPD
$\bar{\beta}$	$3-18$	$5-11$
$\bar{\omega}$	$\lesssim 9.4\times10^{-5}$	$0.2-0.35$
$k_\perp^2\rho_i^2$	$\ll 1^a$	$\ll 1$
$k_\perp^2\rho_s^2$	$\ll 1^a$	$\ll 1$
β_e	$1.5-9.6\times10^{-3}$	$0.7-1.5\times10^{-3}$
$\lambda_\parallel/L_{A,min}$	$\gtrsim 4.5$	$\lesssim 7.5$
ν_{ei}/ω	$2-2400$	$42-114$
$L_{A,min}/\lambda_{mfp,e}$	~ 13	$9-46$
b/B_0	$\lesssim 0.02$	$\lesssim 10^{-4}$

[a] Assuming that Alfvén waves in coronal holes satisfy nearly ideal MHD conditions.

Alfvén waves interact with electrons and ions in the plasma as the waves propagates. The response of the electrons to the wave field is characterized by the dimensionless parameter, $\bar{\beta} = 2v_{te}^2/v_A^2$. The electron thermal speed $v_{te} = \sqrt{T_e/m_e}$, where T_e is the electron temperature in energy units and m_e is the electron mass. The Alfvén speed $v_A = B_0/\sqrt{\mu_0\rho}$, where B_0 is the ambient magnetic field, μ_0 is the permeability of free space, $\rho = (n_i m_i + n_e m_e)$ is the mass density of the plasma, n_i is the ion number density, n_e is the electron number density, and m_i is the ion mass.

In coronal holes, $\bar{\beta} > 1$. As a result, the electrons respond adiabatically to the wave field. We matched the condition of coronal holes $\bar{\beta} > 1$ in LAPD by tuning the parameters such as n, T_e and B_0 (See Table 1).

The wave energy in coronal holes has a wide spectrum. However, most of the wave energy occurs at $\omega \ll \omega_{ci}$, where $\omega_{ci} = qB_0/m_i$ is the angular ion cyclotron frequency, and q is the charge of the ion. Models suggest photospheric fluctuations primarily generate waves at frequencies $f = \omega/2\pi$ between $\sim 0.1-100$ mHz (Cranmer & Van Ballegooijen 2005). The ambient magnetic field in a coronal hole is $\sim$ 0.7 G at a height of 0.15 $R_\odot$ (Morton et al. 2015), where $R_\odot$ is the solar radius. At this height, $\bar{\omega} = \omega/\omega_{ci}$ ranges from $\approx 9.4\times10^{-8} - 9.4\times10^{-5}$. The parameter $\bar{\omega}$ reduces the Alfvén wave speed as ω approaches ω_{ci}. This effect can be seen from the simplified Alfvén wave dispersion relation adopted from Gekelman et al. (1997, 2011),

$$\frac{\omega}{k_\parallel} \approx v_A\sqrt{1-\bar{\omega}^2}, \tag{1}$$

where $\rho_s = c_s/\omega_{ci}$ is the ion sound gyroradius, $c_s = \sqrt{T_e/m_i}$ is the ion sound speed, $k_\parallel = 2\pi/\lambda_\parallel$ is the wave

number parallel to $\mathbf{B_0}$, and $\lambda_\parallel$ is the wavelength along $\mathbf{B_0}$. We minimized the finite frequency correction, $1-\bar{\omega}^2$, by limiting the wave frequency to satisfy $\bar{\omega} \leq 0.35$ near the antenna.

Alfvén wave dynamics can be affected by two-fluid and kinetic effects (Cross 1988; Gekelman et al. 1997; Cramer 2011). One of the parameters that affects two-fluid and kinetic physics is $k_\perp$, which appears in the rigorously derived Alfvén wave dispersion relation through the dimensionless terms $k_\perp^2\rho_\mathrm{i}^2$, $k_\perp^2\rho_\mathrm{s}^2$, and $k_\perp^2\delta_\mathrm{e}^2$ (Gekelman et al. 1997; Cramer 2011; Bose et al. 2019). Here, $k_\perp = 2\pi/\lambda_\perp$ is the wave number perpendicular to $\mathbf{B_0}$, $\lambda_\perp$ is the perpendicular wavelength of Alfvén wave, $\rho_\mathrm{i} = v_\mathrm{ti}/\omega_\mathrm{ci}$ is the ion Larmor radius, $v_\mathrm{ti} = \sqrt{T_i/m_\mathrm{i}}$ is the ion thermal velocity, T_i is the ion temperature, $\rho_\mathrm{s} = c_\mathrm{s}/\omega_\mathrm{ci}$ is the ion sound gyroradius, $\delta_e = c/\omega_\mathrm{pe}$ is the electron skin depth, c is the speed of light, $\omega_\mathrm{pe} = \sqrt{ne^2/m_\mathrm{e}\epsilon_0}$ is the electron plasma frequency, e is the fundamental unit of electrical charge and ϵ_0 is the permitivity of free space.

In coronal holes, there is no measurement of $k_\perp$ of the Alfvén waves, but most of the wave-based heating models invoke ideal MHD (magnetohydrodynamic) conditions, i.e., $k_\perp^2\rho_\mathrm{i}^2$, $k_\perp^2\rho_\mathrm{s}^2$, and $k_\perp^2\delta_\mathrm{e}^2$ are all $\ll 1$ (Gekelman et al. 1997). We used an antenna that excites a large dominant $\lambda_\perp$ to match this condition in LAPD (Gigliotti et al. 2009; Karavaev et al. 2011). In our experiments, the dominant $\lambda_\perp$ of the incident wave is approximately 21.78 cm ensuring that $k_\perp^2\rho_\mathrm{i}^2$, $k_\perp^2\rho_\mathrm{s}^2$, $k_\perp^2\delta_\mathrm{e}^2$ are all $\ll 1$. This value of $\lambda_\perp$ is determined from the wave data using a Fourier-Bessel analysis (Churchill & Brown 1987) as illustrated by Vincena (1999).

The energy in coronal holes is in the magnetic field. The magnetic pressure dominates over thermal pressure, which is represented by the dimensionless parameter $\beta_\mathrm{e} = 2\mu_0 nT_\mathrm{e}/B_0^2$. The value of β_e varies between $\approx 9.6\times10^{-3}$ and 1.5×10^{-3} at low heights in coronal holes (Bose et al. 2019). To match this in LAPD, we adjusted B_0, n, and T_e to produce a value of β_e ranging from $\approx 0.7\times10^{-3}$ to $\approx 1.5\times10^{-3}$.

Alfvén waves encounter a strong v_A gradient at low heights in coronal holes. An estimate of the effect of the gradient on a wave is $\lambda_\parallel/L_\mathrm{A}$ which is also referred to as wave inhomogeneity parameter. L_A is the length scale of v_A in the gradient. This length scale is defined as $v_\mathrm{A}/v'_\mathrm{A}$, where v'_A is the first spatial derivative of v_A. If $\lambda_\parallel/L_\mathrm{A} \gtrsim 1$, the gradient is strong because v_A changes significantly within a wavelength. While if $\lambda_\parallel/L_\mathrm{A} < 1$, the gradient is weak because the variation of v_A within a wavelength is small. In coronal holes, L_A varies spatially at low heights and we have used $L_\mathrm{A,min}$ for scaling purposes, where $L_\mathrm{A,min}$ is the minimum value of the length scale in the gradient region. Note that the length scale attains its minimum value at the strongest part of the gradient. The bulk of the wave energy in coronal holes satisfies the condition $\lambda_\parallel/L_\mathrm{A,min} \gtrsim 4.5$ (Morton et al. 2015; Bose et al. 2019). To match this regime in LAPD, we adjusted B_0, n, and ω to produce $\lambda_\parallel/L_\mathrm{A,min}$ up to 7.5.

Alfvén waves are known to damp due to Coulomb collisions (Cramer 2011). A parameter characterizing the effect of collisions on waves is ν_ei/ω, where ν_ei is the electron-ion collision frequency. The ratio ν_ei/ω is a measure of the number of collisions occuring in a wave period. If $\nu_\mathrm{ei}/\omega \gg 1$, the plasma is collisional for the wave; and if $\nu_{ei}/\omega \ll 1$, it is collisionless plasma. To calculate ν_ei, we use the conventional method from Braginskii (1965),

$$\nu_\mathrm{ei} = 2.9\times10^{-6} n\Lambda T_\mathrm{e}^{-3/2}, \tag{2}$$

where Λ is the Coulomb logarithm (Huba et al. 2016), and ν_ei is in Hz. For coronal hole conditions of $n \sim 2\times10^7$ cm^{-3} and $T_\mathrm{e} \sim 86$ eV $\left(10^6\ \mathrm{K}\right)$ at 0.15 $R_\odot$, we find $\nu_\mathrm{ei} \sim 1.5$ Hz (Morton et al. 2015; Cranmer 2009). Therefore, for wave frequencies ranging from $f \sim 0.1-100$ mHz (Cranmer & Van Ballegooijen 2005), ν_ei/ω varies from ~ 2 to 2400. Hence, at low heights in the v_A gradient region of coronal holes, collisions are sufficient to affect Alfvén wave physics. To match this in the laboratory, we adjusted, ω, n and T_e (see Table 1).

Another estimate of the effect of electron-ion collisions on the Alfvén wave in the gradient region is given by the ratio of the electron mean free path, $\lambda_\mathrm{mfp,e}$, to $L_\mathrm{A,min}$ (Bose et al. 2019). This ratio gives a measure of the number of electron mean free paths within the v_A gradient. The value of $L_\mathrm{A,min}/\lambda_\mathrm{mfp,e}$ in coronal holes is estimated to be ~ 13 (Bose et al. 2019). We match this in LAPD by suitably selecting the range of n, T_e and $L_\mathrm{A,min}$. See Table 1 for representative values of $L_\mathrm{A,min}/\lambda_\mathrm{mfp,e}$ in LAPD.

Lastly, Alfvénic waves with amplitude as high as $b/B_0 \sim 0.02$ were reported in coronal holes McIntosh et al. (2011). In this regime, nonlinear effects may play a role. Following Bose et al. (2019), we restricted our experiment to the low amplitude regime $b/B_0 \lesssim 10^{-4}$ to avoid known nonlinear effects associated with larger amplitude Alfvén waves.

3. EXPERIMENTS

3.1. *Overview*

LAPD was used to produce an ≈ 19 m long cylindrical plasma column (Gekelman et al. 2016). Electromagnets arranged coaxially along the cylindrical vacuum vessel were used to generate a background axial magnetic field,

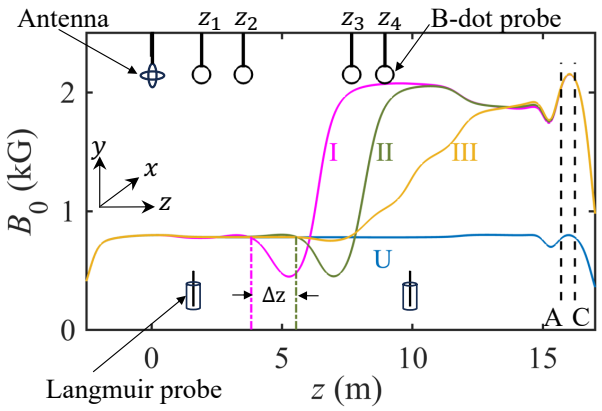

Figure 1. Schematic of the experimental arrangement. The anode (A) and the cathode (C) of the plasma source are at 15.7 and 16.23 m, respectively. The orthogonal ring antenna used to excite Alfvén waves is located at $x = y = z = 0$. The vertical ring of the antenna lies in the yz-plane, while the horizontal ring lies in the xz-plane. The four magnetic field profiles used for the wave experiment (U, I, II, and III) are indicated by different colors. The location of the four B-dot probes are indicated at the top of the figure. A Langmuir probe was used to make measurements at two locations shown at the bottom of the figure. The quantity Δz corresponds to 1.72 m.

B_0. Plasma was formed through electron impact ionization of Helium by applying a discharge voltage between a mesh anode and a LaB_6 cathode located at the far end of the machine, as shown in Fig. 1.

For our experiments, a two cycle linearly polarized Alfvén wave of azimuthal mode number $m = 1$ was excited using an orthogonal ring antenna placed on the cylindrical axis of LAPD at $x = y = z = 0$ (Gigliotti et al. 2009; Karavaev et al. 2011; Bose et al. 2019). Triaxial B-dot probes at $z_1 = 1.92$ m, $z_2 = 3.51$ m, $z_3 = 7.67$ m, and $z_4 = 8.95$ m were used to make wave magnetic-field measurements (Everson et al. 2009; Bose et al. 2018).

We studied reflection of Alfvén waves by varying $\lambda_\parallel$ and $L_{\mathrm{A,min}}$. The wave frequency was changed to vary $\lambda_\parallel$, while different B_0 gradients were employed to alter $L_{\mathrm{A,min}}$. The four B_0 profiles used for the reflection experiments are shown in Fig. 1.

A Langmuir probe was used to measure n and T_e for the gradient cases (Hershkowitz et al. 1989; Bose et al. 2017). The density measurements were calibrated using an interferometer that measured line-integrated density. For the gradient cases, the estimated plasma parameters at $z = 1.6$ m are $n \sim 5 - 8 \times 10^{12}$ cm^{-3} and $T_e \sim 3$ eV, while at $z = 9.9$ m, they are $n \sim 7 - 9 \times 10^{12}$ cm^{-3} and $T_e \sim 10$ eV. We do not have Langmuir probe measurements for the uniform B_0 case; the estimated n from the Alfvén wave dispersion relation is $\sim 8 \times 10^{12}$ cm^{-3}.

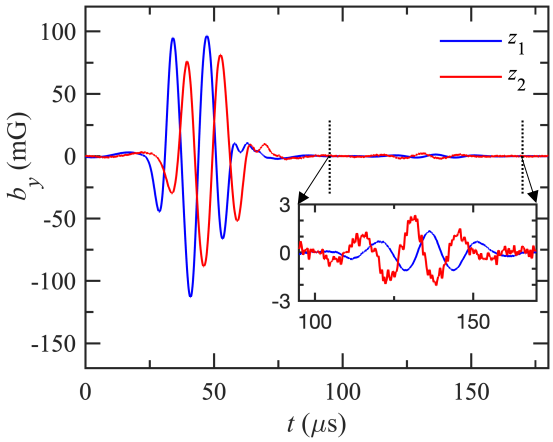

Figure 2. The time variation of the y component of the wave magnetic field, b_y. The measurements were made on the axis of LAPD at z_1 and z_2 for case U. Initially, the wave at z_1 (blue) occurs before the wave at z_2 (red), suggesting that the wave is propagating away from the antenna. The waveform within the dotted lines, highlighted in the inset figure, is due to reflection from the cathode and propagating towards the antenna.

3.2. *Detection of an Alfvén wave reflected from a v_A gradient*

We performed a number of wave experiments to detect a reflected Alfvén wave from a v_A gradient and validate the findings. We first studied the wave propagation through a uniform B_0 as a control case (profile U in Fig. 1). Second, we excited an Alfvén wave in the presence of a strong v_A gradient (profile I in Fig. 1) and detected a reflected wave from the v_A gradient. Third, we pushed the v_A gradient further from the antenna (profile II in Fig. 1) and found the phase difference between the incident and reflected wave increased, confirming that the v_A gradient is the reflector. Fourth, we weakened the v_A gradient significantly (profile III in Fig. 1); we could not find a reflected wave from this gradient, proving that reflection is a gradient-driven effect. In the subsubsections below, we describe the results and analysis of these experiments using an ≈ 76 kHz incident wave as an example.

3.2.1. *Alfvén wave in uniform B_0*

Figure 2 shows the wave magnetic field time series recorded by B-dot probes at z_1 and z_2 for gradient U. Initially, the peaks and troughs of the wave signal at z_1 leads z_2, which is consistent with an incident wave propagating in the $+z$ direction. Some time after the incident wave in Fig. 2, we see a much smaller wave in the region between the dotted lines. The signal of this smaller wave is observed at z_2 before z_1, indicating the waveform is propagating in the $-z$ direction, towards the antenna.

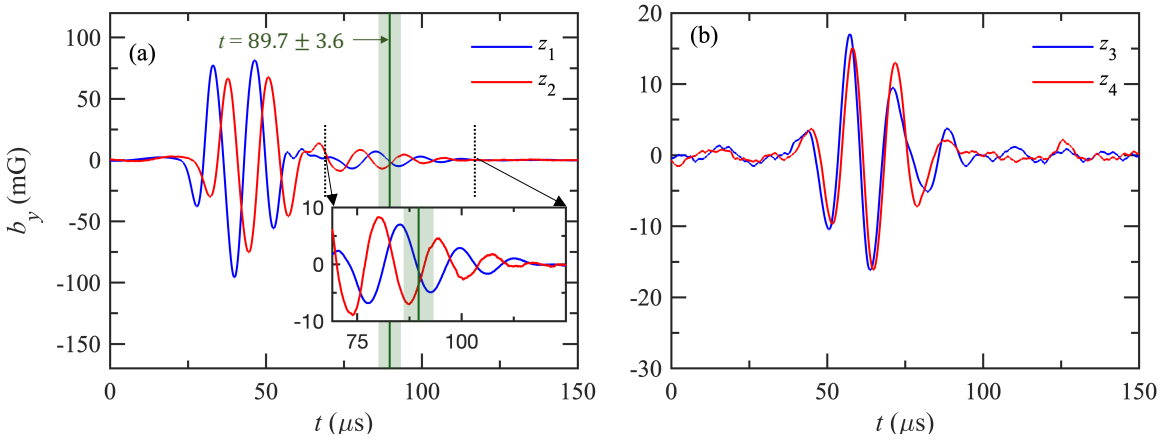

Figure 3. The b_y time series for gradient I as measured on the axis of LAPD (a) on the low field side at z_1 and z_2, and (b) on the high field side at z_3 and z_4. The inset figure in (a) shows the waveform propagating towards the antenna on the low field side. The green line and shaded region in (a) represent the expected time for a wave refelcted from the cathode to arrive at z_2.

Our analysis suggests that the smaller wave signal is reflected from the plasma source at the far end of LAPD. Furthermore, reflection introduces an additional 180° phase difference between the reflected and incident wave; the smaller signal in Fig. 2 has three peaks and two troughs, while in the incident wave has two peaks and three troughs. We performed time-of-flight calculations using the logic that if the smaller wave at z_1 is reflected from the plasma source, then the time lag between the incident and the inverted smaller wave should be equal to twice the time of flight of the incident wave from z_1 to the plasma source. The time lag ($t^{\rm U}_{\rm lag}$) between the incident and the smaller waves obtained from their phase difference at z_1 is 95.3 ± 0.4 μs. The error bar represent the 1σ uncertainty obtained by calculating the standard deviation of the time lag measured at various radial locations. The time of flight ($t^{\rm U}_{\rm tof}$) of the incident wave from z_1 to the plasma source determined by dividing the distance between z_1 and the cathode, 14.31 m, by the velocity of the wave. The velocity of the wave is $3 \pm 0.1 \times 10^5$ m s^{-1}, as determined by dividing the distance between z_1 and z_2 by the time lag between the wave signals at those two locations. Therefore, $t^{\rm U}_{\rm tof}$ is 47.7 ± 1.6 μs. Hence, $t^{\rm U}_{\rm lag}$ agrees with $2t^{\rm U}_{\rm tof}$, indicating that the smaller wave has been reflected from the plasma source. Our findings agree with previous experiments where physical objects in the plasma, such as metal and insulator plates, were found to reflect Alfvén waves (Leneman 2007).

3.2.2. *Wave reflection from a strong $v_{\rm A}$ gradient*

We introduced a strong $v_{\rm A}$ gradient between the antenna and the far end of LAPD and detected a wave reflected from the $v_{\rm A}$ gradient. The minimum value of the $v_{\rm A}$ length scale within the gradient was $L_{\rm A,min} = 0.74$ m. The wave magnetic field data before the gradient is given in Fig. 3(a). Initially, the peaks and troughs of the wave signal at z_1 leads z_2, which is expected for an incident wave. However, in the region between the dotted lines, a small wave signal is observed at z_2 before z_1, suggesting the wave is propagating in the $-z$ direction. This is likely due to a partial superposition of waves reflected from gradient I and the plasma source, as we explain shortly. Here we remind the reader that since $v_{\rm A} \propto B_0$, the time window for the wave reflected by the plasma source at z_1 and z_2 for the strong $v_{\rm A}$ gradient and uniform B_0 profile will be different as the values of B_0 near the plasma source is different in the two cases.

In order to help disentangle wave reflection from the gradient from wave reflection by the plasma source, we also measured the wave magnetic field on the high field side at z_3 and z_4 (Fig. 3(b)). The first two peaks and troughs at z_3 leads z_4, which is consistent with wave propagation in the $+z$ direction. However, the third trough of z_3 lags z_4, suggesting the presence of a wave reflected from the far end in the measured signal. The amplitude of the third trough at z_4 is also more than at z_3, suggesting constructive interference between waves travelling in the $+z$ (incident) and $-z$ (reflected from far end) directions. The presence of a far-end reflected wave is also supported by the amplitude of the third peak at z_4, which is greater than z_3. This observation suggests that the far-end reflected wave may have reached z_4 around $t = 68.3 \pm 3.5$ μs. The upper limit corresponds to the time of the second peak at z_4, where we observe a signature of a reflected wave from the far end. The lower limit refers to the time of the second trough at z_4 where we do not observe a sign of reflection from the far end.

Building on this, we put forward two sets of analyses that imply that the first cycle of the wave propagating in the $-z$ direction at z_2 is reflected from gradient I only

and does not have any contribution due to far-end reflection. First, we estimate the time at which a wave reflected from the plasma source will reach z_2. The arrival time of the reflected wave from the source is equal to 68.3 ± 3.5 μs plus the time of flight of the wave from z_4 to z_2. Since the speed of Alfvén wave propagation in the $+z$ and $-z$ direction is the same, the time of flight of an Alfvén wave from z_4 to z_2 (i.e., the $-z$ direction) is determined from the phase difference of the incident wave (i.e., the $+z$ direction) between z_2 and z_4. The inferred time of flight is 21.4 ± 0.7 μs. Therefore, the part of the waveform at z_2 beyond $t = 89.7 \pm 3.6$ μs may contain a contribution from a wave reflected from the plasma source. Hence, the first cycle of the waveform in the inset graph of Fig 3(a) is not affected by reflection from the source.

Next, we show that the location of reflection of the first cycle of the wave propagating in the $-z$ direction at z_2 is within gradient I. Since gradient I is located between z_2 and z_3, for the first cycle to be reflected from the gradient I, the time lag between the incident and reflected wave at z_2, $t^{\rm I}_{\rm lag}$, must be less than the twice the time of flight of the wave from z_2 to z_3, $2t^{\rm I}_{\rm tof}$. We used the results of the simulations given in Section 4 to correlate the phases of incident and gradient-reflected wave. Simulations showed that reflection from a $v_{\rm A}$ gradient introduces a 180° phase difference between the incident and the reflected wave. In addition, the simulations also suggest that the leading low amplitude trough of the incident Alfvén wave may not produce a sufficiently strong reflected wave to be experimentally detectable. The subsequent peaks and troughs of the incident Alfvén wave, though, are predicted to produce a detectable reflected wave. Therefore, in Fig. 3(a), the first peak of the incident wave should correspond to the first trough of the wave moving in the $-z$ direction if it is reflected from the $v_{\rm A}$ gradient. The time lag between the first peak of the incident wave and the first trough of the reflected wave is $t^{\rm I}_{\rm lag} = 36.0 \pm 0.2$ μs. The time of flight of the wave from z_2 to z_3 obtained by comparing the phase difference between the $+z$ propagating part of the wave at z_2 and z_3 is $t^{\rm I}_{\rm tof} = 20.4 \pm 0.7$ μs. Hence, $t^{\rm I}_{\rm lag} < 2t^{\rm I}_{\rm tof}$ indicating that the source of reflection is located within gradient I. This experimental finding is supported by our simulations described in Section 4.

3.2.3. *Wave reflection experiment by changing the location of a strong $v_{\rm A}$ gradient*

To further confirm experimentally that gradient I is indeed reflecting an Alfvén wave, we moved the gradient further away from the antenna and checked if the time lag between the incident and reflected wave increased accordingly. We refer to this shifted gradient as gradient II. A comparison of the wave signal at z_2 for gradients I and II is presented in Fig. 4.

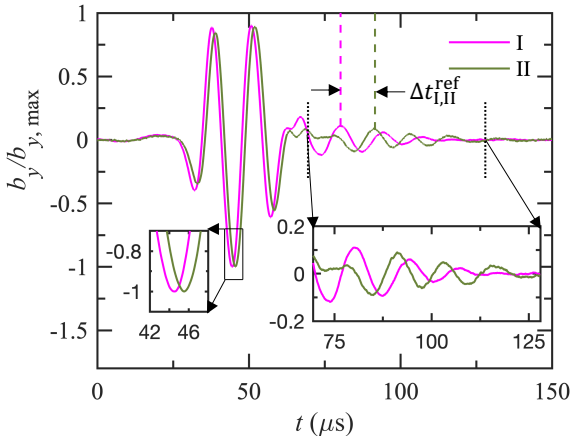

Figure 4. Comparison of the normalized b_y time series measured at z_2 on the axis of LAPD before (magenta) and after (green) moving the gradient away from the antenna. The inset figure on the right highlights the significant phase difference observed between the reflected waves due to moving the gradient away from the antenna. The inset figure on left shows that there is a minor phase difference between the incident waves of the two cases.

We performed further analysis to quantitatively show that the phase difference between the reflected wave from gradients I and II agrees with the extra distance traversed by the wave to reach gradient II and return. The investigation was done using the first wave cycle propagating in $-z$ direction for both gradients. This is because an analysis for gradient II following the methodology in subsection 3.2.2 that was used for gradient I showed that the reflector for the first cycle is located within the gradient II region. The time lag between waves reflected from I and II is $t^{\rm I,II}_{\rm lag} \approx 2\Delta z/v_{\rm ph,\parallel}$, where $\Delta z = 1.72$ m is the distance between gradients I and II (Fig. 1), and $v_{\rm ph,\parallel}$ is the phase velocity of the Alfvén wave parallel to B_0 in the low-field side. We find $v_{\rm ph,\parallel} = 3.3 \pm 0.1 \times 10^5$ m s^{-1}, as determined by dividing the distance between z_1 and z_2 by the phase difference of the incident wave at z_1 and z_2. This gives, $t^{\rm I,II}_{\rm lag} \approx 10.4 \pm 0.3$ μs. The phase difference between the reflected wave from I and II is $\Delta t^{\rm ref}_{\rm I,II} \approx 11.0 \pm 0.2$ μs. In Fig. 4, we find a minor phase offset between the incident waves for cases I and II possibly due to small difference in density. This minor phase offset adds to the phase difference between the reflected waves from the two gradients. Correcting for the phase difference between incident waves, we find $\Delta t^{\rm ref}_{\rm I,II} \approx 10.0 \pm 0.3$ μs. Thus, $t^{\rm I,II}_{\rm lag}$ closely agrees with $\Delta t^{\rm ref}_{\rm I,II}$ further confirming that the gradient is reflecting

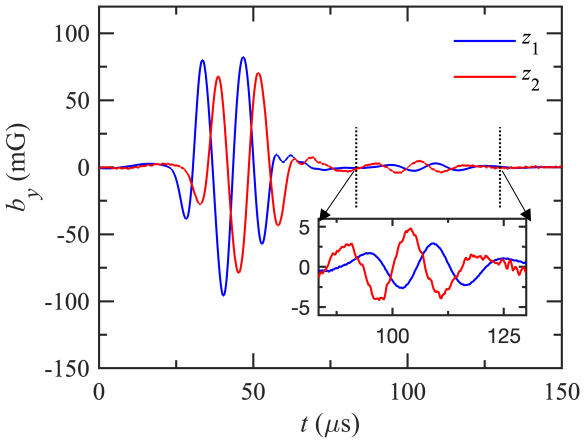

Figure 5. The time variation of b_y for gradient III measured on the axis of LAPD at z_1 and z_2. Initially, the peaks and troughs of the wave signal at z_1 leads z_2, which is consistent for a wave propagating in the $+z$ direction. However, some time after the incident wave, the smaller wave reflected from the far end is seen propagating in the $-z$ direction.

Alfvén waves. This experimental finding is supported by our simulation discussed in Section 4.

3.2.4. *Alfvén wave incident on a weak v_A gradient*

As a further test to prove that the first cycle of the reflected wave in Fig. 3(a) is a gradient driven effect, we weakened the v_A gradient and repeated the experiment. The $L_{A,min}$ within the gradient was 3.24 m. The wave magnetic field data at z_1 and z_2 for III is shown in Fig. 5. Initially, the troughs and peaks of the wave signal at z_1 leads z_2, which is consistent for a wave propagating in the $+z$ direction. However, some time after the incident wave in Fig. 5, we see a much smaller wave in the region between the dotted lines. This small wave is propagating in the $-z$ direction, as the peaks and troughs of the small wave at z_2 leads z_1.

Analysis shows that the small wave is reflected from the plasma source of LAPD and that there is no signature of the wave being reflected from the gradient. For the small wave to be reflected from the source, the time lag (t^{III}_{lag}) between the incident and small wave at z_1 should be equal to twice the time of flight (t^{III}_{tof}) of the wave from the z_1 to the plasma source. The t^{III}_{lag} measured by cross-correlating the incident and small wave after accounting for 180° phase shift caused by reflection is 67.2 ± 1.5 μs. The time of flight calculated using $t^{III}_{tof} = \int_{z=z_1}^{z=16.3} dz / \int_{z=z_1}^{z=16.3} v_A\, dz$ is 35.7 ± 1.9 μs. Here, the z dependence of B_0 primarily causes an axial variation of v_A as $v_A \propto B_0$, while a minor variation in n doesn't effect v_A much as $v_A \propto 1/\sqrt{n}$. Therefore, t^{III}_{lag} agrees with $2t^{III}_{tof}$ to within the measurement uncertainty, proving that the small wave is reflected from the plasma source. Since we do not observe any other wave between the incident wave and the small source-reflected wave in Fig. 5, we conclude that gradient III does not reflect Alfvén waves. This experimental finding is supported by our simulations, which shows that gradient III does not reflect (see Section 4).

3.3. *Dependence of reflected Alfvén wave energy on the v_A inhomogeneity*

We determined the coefficient of reflection, $\mathcal{R}$, to quantify the effectiveness of a v_A gradient in reflecting Alfvén waves. As a first step for determining $\mathcal{R}$, we calculate the energy of the incident wave and of the wave reflected from the v_A gradient. The energy, $\mathcal{E}$, of an Alfvén wave is obtained by integrating the Poynting vector of the wave and $\mathcal{E}$ is given by

$$\mathcal{E} = \int \left(\iint S_{\parallel}\, dxdy \right) dt, \tag{3}$$

where $S_{\parallel} \approx \frac{1}{4\pi} b^2 v_{ph,\parallel}$ is the energy flux along $\mathbf{B_0}$ (Bose et al. 2019). The spatial integration is carried out over the xy cross section of LAPD, and the integration in time, t, is carried out over the duration of the wave train.

$\mathcal{R}$ is obtained from $\mathcal{E}$ using

$$\mathcal{R} = \frac{\Gamma_r}{\Gamma_i} = \frac{\mathcal{E}_r / t_{dur,r}}{\mathcal{E}_i / t_{dur,i}} = \frac{\left[\int \left(\iint b_r^2\, dxdy\right) dt\right] / t_{dur,r}}{\left[\int \left(\iint b_i^2\, dxdy\right) dt\right] / t_{dur,i}}, \tag{4}$$

where Γ is the wave power, t_{dur} is the time duration of the wave train, and subscripts "i" and "r" refer to incident and reflected wave, respectively. The quantity $t_{dur,i}$ consist of the initial ramp-up period and the first full cycle of the incident wave, while $t_{dur,r}$ is the period of first cycle of the reflected wave. The definition of $t_{dur,i/r}$ is motivated by simulation results given in Fig. 8d where a single cycle of the reflected wave is produced by an incident wave comprising of an initial ramp-up followed by a full cycle.

3.3.1. *Measurement of coefficient of reflection at z_2*

The values of $\mathcal{R}$ calculated by taking the ratio of the reflected to incident wave power at z_2 is given by color filled symbols in Fig. 6, where the magenta and yellow colored data points represent measurements for gradients I and III, respectively. $\mathcal{R}$ is presented as a percentage by multiplying Eq. 4 by 100. For convenience we have referred to $\mathcal{R}$ measured at z_2 as $\mathcal{R}_{z_2}$.

$\mathcal{R}_{z_2}$ data points for gradient I shows that longer wavelength waves are reflected more strongly from a v_A gradient than shorter wavelengths. The wavelengths were changed by varying the wave frequency. For the longest wavelength, $\lambda_{\parallel} = 5.6 \pm 1.2$ m ($\lambda_{\parallel}/L_{A,min} = 7.5 \pm 1.6$),

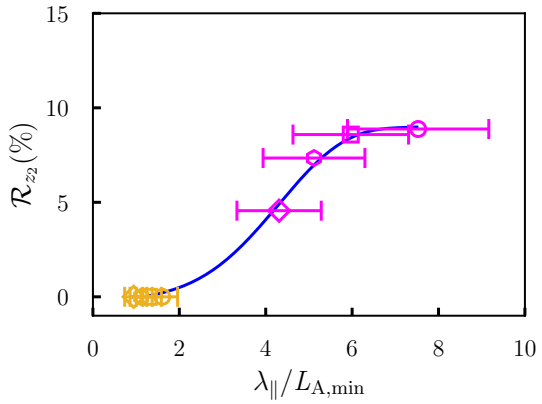

Figure 6. The variation of the coefficient of reflection of Alfvén wave measured at z_2 vs. $\lambda_\parallel/L_{\rm A,min}$. The vertical error bars are smaller than the symbol size. The value of $\lambda_\parallel$ was changed by altering the wave frequency. The different wave frequencies are represented by various symbols, circle = 61 kHz, square = 76 kHz, hexagon = 89 kHz, and diamond = 104 kHz. $L_{\rm A,min}$ was varied by changing the B_0 gradient. The magenta and yellow color corresponds to gradients I and III, respectively. The continuous blue line is the most probable function that connect the data points as per Gaussian process regression.

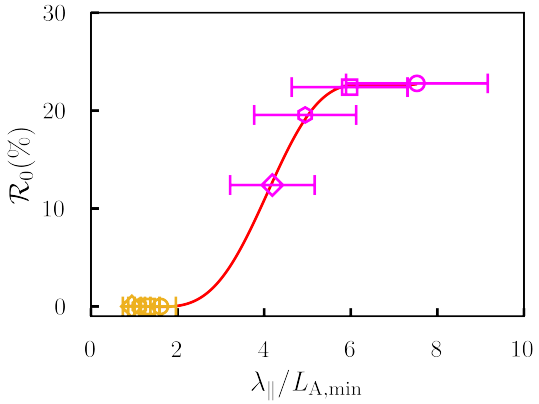

Figure 7. The variation of the coefficient of reflection of Alfvén wave estimated at the site of the reflector in the gradient, $\mathcal{R}_0$, vs. $\lambda_\parallel/L_{\rm A,min}$. The vertical error bars are smaller than the symbol size. The continuous red line is the most probable function that connect the data points as per Gaussian process regression.

and $\mathcal{R}_{z_2}$ is $\approx 9\%$. For the shortest wavelength, $\lambda_\parallel = 3.2 \pm 0.7$ m ($\lambda_\parallel/L_{\rm A,min} = 4.3 \pm 1$ m), and $\mathcal{R}_{z_2}$ is 4.6%. Note, the errorbar of $\lambda_\parallel$ is due to uncertainty in frequency measurement which in turn is due to the finite temporal length of the incident wave. We estimated the frequency uncertainty using the full width at half maximum of the frequency peak in the Fourier spectrum of the incident wave.

A comparison of $\mathcal{R}_{z_2}$ data points for gradients I and III suggests that the length scale of the $v_{\rm A}$ gradient affects wave reflection. $\mathcal{R}_{z_2}$ is zero for gradient III, as the measurement of wave magnetic field along the x axis spanning the width of the plasma column at $y = 0$ did not reveal any signature of a reflected wave from the $v_{\rm A}$ gradient. However, $\mathcal{R}_{z_2}$ is non-zero for I. The key difference between I and III are their values of $L_{\rm A,min}$ because $\lambda_\parallel$ for both gradients lie in the same range. $L_{\rm A,min}$ for I and III are 0.74 m and 3.24 m, respectively. Note that $L_{\rm A,min}$ signifies the degree of inhomogeneity of a $v_{\rm A}$ gradient and a small $L_{\rm A,min}$ indicates a strong gradient.

The blue curve in Fig. 6 showing the variation of $\mathcal{R}_{z_2}$ vs. $\lambda_\parallel/L_{\rm A,min}$ as predicted by Gaussian process regression (GPR), a class of machine learning algorithms (Rasmussen 2005). GPR is a Baysean non-parametric regression technique that predicts a probability distribution over possible functions that fit a set of discrete data points. The blue curve in Fig. 6 gives mean of the probability distribution i.e., most probable characterization of the data (Pedregosa et al. 2011; Bose et al. 2022).

3.3.2. *Estimating coefficient of reflection in the gradient*

The values of $\mathcal{R}_{z_2}$ in Fig. 6 are the lower limit of the coefficient of reflection. This is because the incident Alfvén wave damps as it propagates from z_2 to the location of the reflector in the gradient, causing the incident wave energy to be smaller at the location of the reflector than at z_2. Similarly, the reflected wave damps as it propagates from the site of the reflector in the gradient, causing the reflected wave energy to be smaller at z_2. As a result, the incident wave energy is overestimated while the reflected wave energy is underestimated at z_2 compared to the corresponding energies at the site of the reflector in the gradient.

We have used a simple model to estimate the incident and reflected wave energy at the site of the wave reflector to make a zeroth order correction to the directly measured values of $\mathcal{R}_{z_2}$. In the model, the incident wave energy at z_2 ($\mathcal{E}_{\rm i}$) is related to the incident wave energy at the site of wave reflector ($\mathcal{E}_{\rm i,0}$) by

$$\mathcal{E}_{\rm i,0} \approx \mathcal{E}_{\rm i} \exp\left(-2\Delta z/d\right), \tag{5}$$

where Δz is the distance between z_2 and location of the reflector, and d is the collisional damping length of Alfvén wave, i.e., the length over which the Alfvén wave amplitude decreases to $1/e$ of its initial value. Note, the factor 2 appears in the exponential term of Eq. (5) because $\mathcal{E} \propto b^2$ and the damped amplitude of $b \propto \exp\left(-\Delta z/d\right)$. Similarly, the reflected wave energy at the reflector ($\mathcal{E}_{\rm r,0}$) and at z_2 ($\mathcal{E}_{\rm r}$) are related by

$$\mathcal{E}_{\rm r} \approx \mathcal{E}_{\rm r,0} \exp\left(-2\Delta z/d\right). \tag{6}$$

Therefore, the coefficient of reflection at the site of the reflector ($\mathcal{R}_0$) is given by

$$\mathcal{R}_0 \approx \frac{\mathcal{E}_{\mathrm{r},0}/t_{\mathrm{dur,r}}}{\mathcal{E}_{\mathrm{i},0}/t_{\mathrm{dur,i}}} \approx \mathcal{R}_{z_2} \exp\left(4\Delta z/d\right). \tag{7}$$

The collisional damping length is estimated using the two-fluid dispersion relation of Alfvén wave for uniform plasma in the $\bar{\beta} \gg 1$ limit, (Vranjes et al. 2006; Gigliotti et al. 2009; Bose et al. 2019)

$$\omega^2 - k_\parallel^2 v_\mathrm{A}^2 \left(1 - \bar{\omega}^2 + k_\perp^2 \rho_\mathrm{s}^2\right) + i\omega k_\perp^2 \delta_e^2 \nu_e = 0. \tag{8}$$

This quadratic equation can be solved algebraically, and the imaginary root, $k_{\mathrm{Im},\parallel}$, gives the damping length,

$$\begin{aligned} d &= \frac{1}{k_{\mathrm{Im},\parallel}} \\ &= \frac{\sqrt{2} v_\mathrm{A}}{\omega} \left[\frac{\sqrt{1 + k_\perp^4 \delta_e^4 \left(\nu_e/\omega\right)^2} - 1}{1 - \bar{\omega}^2 + k_\perp^2 \rho_\mathrm{s}^2}\right]^{-1/2}. \end{aligned} \tag{9}$$

The dominant perpendicular wavelength of the incident wave, $\lambda_\perp = 21.78$ cm. The average value of the plasma parameters between z_2 and the reflector are employed for estimating d using Eq. 9. The site of reflector is taken to be location of the strongest part of the v_A gradient, which is at $z = 6.2$ m, therefore, $\Delta z = 2.7$ m. The average B_0 between z_2 and $z = 6.2$ m is 623 G. The values of d for 61, 76, 89 and 104 kHz waves are 11.4, 11.2, 11, and 10.6 m, respectively.

The resulting value of $\mathcal{R}_0$ has a monotonic variation with respect to $\lambda_\parallel/L_{\mathrm{A,min}}$ as shown in Fig. 7. The data points are shown by symbols while the red curve is most probable characterization of the data points as per GPR. The $\mathcal{R}_0$ vs. $\lambda_\parallel/L_{\mathrm{A,min}}$ curve shows that as the inhomogeneity increases, so does the reflection of Alfvén waves.

The values of $\mathcal{R}_0$ are approximate quantities as we estimated d of the Alfvén wave in the gradient using the dispersion relation for a uniform plasma. A comprehensive analysis to accurately determine d in a strong non-WKB gradient relevant to our experiments is beyond the scope of this paper. However, past experiments of Bose et al. (2019) does provide an insight on the damping of Alfvén waves in a strong non-WKB gradient. They found the energy reduction of an Alfvén wave in a strong non-WKB gradient to be more than in an almost uniform plasma suggesting that the damping length is smaller (i.e. damping is more pronounced) in the gradient than in the uniform case. This implies that for the uniform plasma the values of d used to calculate $\mathcal{R}_0$ overestimates the damping length in the gradient and thus underestimates $\mathcal{R}_0$. Therefore, $\mathcal{R}_0$ in Fig. 7 is likely to be a lower bound on the coefficient of reflection after correcting for collisional damping.

4. SIMULATIONS

4.1. *Overview*

We employ the five-moment, two-fluid model (Hakim et al. 2006; Wang et al. 2015, 2020) within the `Gkeyll` simulation framework to model Alfvén-wave reflection in LAPD. The five-moment model evolves equations for density, momentum, and isotropic pressure for each species, which are coupled through Maxwell's equations, and includes the displacement current. We model the full LAPD domain in Cartesian coordinates with reflecting boundary conditions in each dimension, $-0.6\ \mathrm{m} \leq x,\ y \leq 0.6$ m and $-10\ \mathrm{m} \leq z \leq 18$ m, and employ $n_x = n_y = 64$ and $n_z = 700$ cells. We initialize a Helium plasma, $m_i = 4m_p$, with $m_p = 1.67 \times 10^{-24}$ g and a reduced mass ratio, $m_i/m_e = 100$, uniform temperatures and densities based on fiducial values from the experiments, $T_e = 7$ eV, $T_e/T_i = 5$, and $n = n_e = n_i = 7 \times 10^{12}$ cm^{-3}. The speed of light for simulations is taken to be $c \simeq 9.5 \times 10^6$ m s^{-1}. Three background, axial magnetic field profiles are employed corresponding to field profiles U, I, and III in Fig. 1. We drive the plasma with a model of the Arbitrary Spatial Waveform (ASW) antenna placed at $z = 0$ m (Thuecks et al. 2009; Drake et al. 2013). The antenna parameters are $J = 10$ kA m^{-3}, $f_{\mathrm{ant}} = 76.4$ kHz, and $\lambda_{\perp\mathrm{ant}} = 21.78$ cm, which drives an Alfvén wave with $\lambda_\parallel \simeq 4.4$ m. The antenna is driven for a time $t_{\mathrm{drive}} = 1.5/f_{\mathrm{ant}}$. This includes ramping up and down periods, each of length $t_{\mathrm{ramp}} = 0.25/f_{\mathrm{ant}}$. We note that we both extend the LAPD-model domain to $z = -10$ m and flatten the background magnetic field gradient in this region to reduce spurious reflections from behind the antenna.

4.2. *Results*

4.2.1. *Alfvén wave through uniform B_0*

Fig. 8(a) shows the wave propagation along the cylindrical axis of LAPD in the tz-plane for gradient U. The color gives the y-component of the wave magnetic field, which in turn also indicates the phase of the wave. The slope of the band traced by the phase of the wave indicates the propagation direction of the wave; positive and negative slope corresponds to $+z$ and $-z$ direction, respectively. In Fig. 8(a), the slope of the band traced by the phase of the wave is positive, consistent for an incident wave propagating away from the antenna. Fig. 8(b) shows the time variation of the incident wave at $z = 3.5$ m. Unlike the experiment, we do not see a wave reflected from the far end in the time series data because the simulation was carried out up to $\approx 78\ \mu s$, and the wave reflected from the far end requires a longer time to reach $z = 3.5$ m.

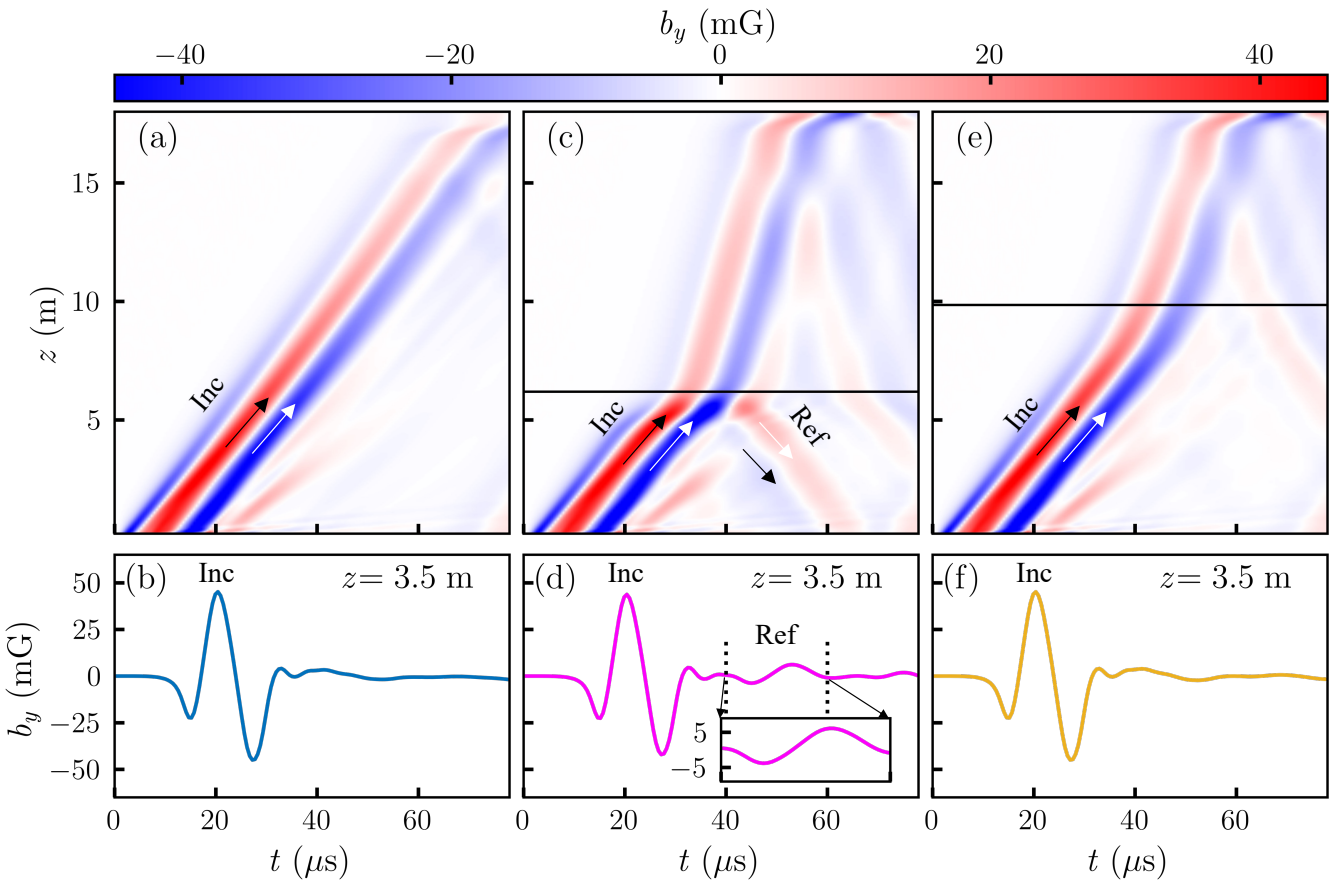

Figure 8. (Top row) 2-D color plots of $b_y(x = y = 0)$ displaying the propagation of the incident (Inc) Alfvén wave and its reflection (Ref) in the tz-plane for gradient (a) U, (c) I, and (e) III. The z axis extend from 0.2 to 18 m, while the t axis ranges from 0 to 78 μs. The deep red color implies that the oscillating b_y is at its maximum positive value of the wave peak, while the deep blue indicates b_y is at the minimum of the wave trough. The arrows trace the phase of the wave. The black horizontal line in (c) and (e) show the z location of $L_{\rm A,min}$ in the $v_{\rm A}$ gradient. (Bottom row) The time variation of b_y obtained by taking a horizontal cut at $z = 3.5$ m for gradients (b) U, (d) I, and (f) III. The inset figure in (d) show b_y vs. t between 40 to 60 μs.

4.2.2. *Alfvén wave reflection from a strong $v_{\rm A}$ gradient*

Fig. 8(c) shows the wave propagation in the tz-plane for gradient I, where we observe experimentally wave reflection from the $v_{\rm A}$ gradient. Initially, from $t = 0$ to $\lesssim 40$ μs and $z \lesssim 5$ m, the wave propagates in $+z$ direction as expected for an incident wave. Upon reaching the gradient region, where $L_{\rm A} \approx L_{\rm A,min}$, a portion of the incident wave is reflected. The negatively sloped arrows trace the phases of the wave reflected from the $v_{\rm A}$ gradient.

We observe that reflection from a $v_{\rm A}$ gradient introduces a 180° phase difference between the wave magnetic field of the incident and the reflected wave. In Fig. 8(c), the deep blue band of the incident wave, marked by the positively sloped white arrow, correlates to the negatively sloped red band (reflected wave), marked by the negatively sloped white arrow. Similarly, the positively sloped deep red band of the incident wave corresponds to the negatively sloped blue band of the reflected wave, as shown by follow the black arrows in Fig. 8(c). The change in the color between the corresponding phases of the incident and the reflected wave represents a 180° phase difference. We performed a second test to check the phase difference. Simulations using an incident wave having only a strong negative b_y (i.e. no strong positive b_y) gave rise to a reflected wave with only a positive b_y, further demonstrating a 180° phase difference between incident and reflected wave due to reflection. See Appendix A for the additional details on this second test.

The time variation of b_y before the gradient at $z =$ 3.5 m in Figs. 8 (c) and (d) show that the first low amplitude trough of the incident wave does not produce a strong detectable reflected wave. The reasons for this observation may be related to the process associated with Alfvén wave reflection at the boundary, such as establishing currents at the boundary to support a re-

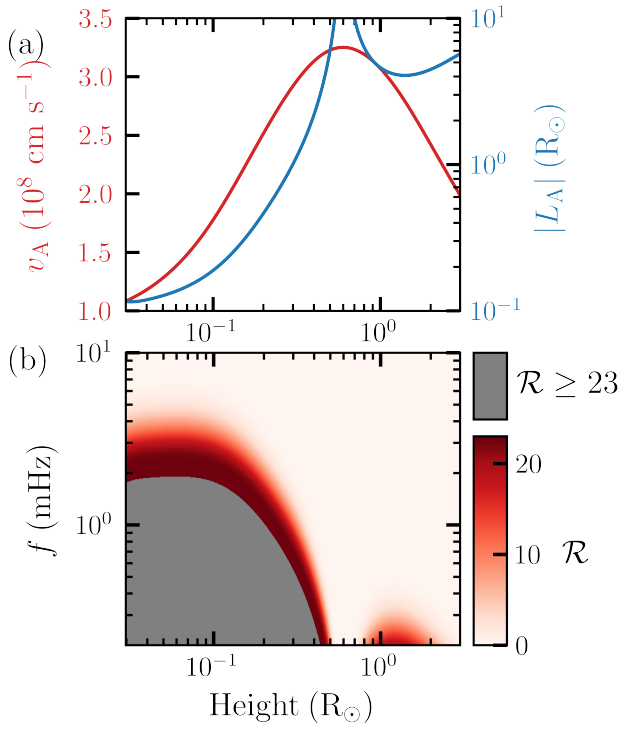

Figure 9. (a) The variation of Alfvén speed, v_A, and length scale of the v_A gradient in a coronal hole vs. height from the surface of the Sun. (b) A colormap showing the estimated coefficient of reflection, $\mathcal{R}(\%)$, for different wave frequencies $(0.2 - 10$ mHz) at different heights above the surface of the Sun in a coronal hole. Note that Alfvén waves are reflected strongly at low heights ($\lesssim 0.13$ R$_\odot$) where v_A gradient is strong (see main text). The words "strong reflection" in this context implies wave reflection that may be enough to generate sufficient heating of the plasma via the wave turbulence mechanism.

flected Alfvén wave. A discussion on the interaction of the Alfvén wave with the v_A gradient boundary is beyond the scope of this paper and will be discussed elsewhere.

4.2.3. *Alfvén wave incident on a weak v_A gradient*

Fig. 8(e) shows the wave propagation in the tz-plane for case III, i.e., the B_0 profile with gradient III. We do not observe any wave reflection from the v_A gradient, but the transmitted wave is reflected from the far end of the simulation domain. The b_y time series data in Fig. 8(f) only shows a well-formed incident wave and does not exhibit any signature of a reflected wave from the v_A gradient.

5. DISCUSSION

Our experimental results have implication on the heating of coronal holes. A significant temperature increase of coronal hole plasma occurs at low heights (Ko et al. 1997; Landi 2008), a region where v_A is highly non-uniform. The spatial variation of v_A is shown by the red curve in Fig. 9(a). We used approximate fits of density and magnetic field given by Cranmer & Van Ballegooijen (2005) to calculate v_A.

A comparison of the wave inhomogeneity parameter $(\lambda_\parallel/L_A)$ for a coronal hole with that of the laboratory suggest that $\mathcal{R}$ can be greater than 23% at low heights. The spatial variation of v_A and L_A in a coronal hole are given by the red and blue curves, respectively, in Fig. 9(a). The $\lambda_\parallel$ at different heights in a coronal hole for various wave frequencies f, can be estimated using $\lambda_\parallel = v_A/f$. The values of f vary from 0.2 to 10 mHz (Morton et al. 2015). The resulting values of $\lambda_\parallel/L_A$ were used to obtain estimates of $\mathcal{R}$ for a coronal hole by comparing $\lambda_\parallel/L_A$ of a coronal hole with $\lambda_\parallel/L_{A,\min}$ of the laboratory (red curve in Fig. 7). Fig. 9(b) shows $\mathcal{R}$ for different values of f at various heights above the surface of the Sun. The different shades of red show the values of $\mathcal{R}$ from 0 to 23%, while the grey indicates $\mathcal{R} \geq 23\%$. The reason for using the grey color is that in a portion of the frequency-height plane the coronal hole values of $\lambda_\parallel/L_A$ are greater than the maximum value of $\lambda_\parallel/L_{A,\min} = 7.5$ attained in the laboratory. Since, the coefficient of reflection has a monotonic dependence on $\lambda_\parallel/L_{A,\min}$ in the laboratory with a maximum value of 23% we assumed that $\mathcal{R}$ is $\geq 23\%$ in a coronal hole for $\lambda_\parallel/L_A > 7.5$.

A comparison of the data in Fig. 9b with solar observations and solar simulations suggests that wave reflection from a smooth v_A gradient may be sufficient to significantly heat the plasma at low heights up to 0.13 R$_\odot$ in coronal holes via the wave turbulence model. Solar observation suggest that waves have sufficient energy to heat a coronal hole (McIntosh et al. 2011). Furthermore, measurement of the wave frequency spectrum by Morton et al. (2015) indicates that bulk of the wave energy occur at frequencies below ~ 3 mHz in a coronal hole. Simulations of Asgari-Targhi et al. (2021) suggests that a reflection coefficient of $\sim 10\%$ may be sufficient to heat the plasma at heights below 3 R$_\odot$ in coronal holes. They invoked density fluctuations to reflect $\sim 10\%$ of the wave power. However, our laboratory results suggest that a smooth v_A gradient relevant to low heights in coronal holes can reflect more than 10% of wave power. In Fig. 9(b) $\mathcal{R}$ is greater than 10% for $f \leq 3$ mHz for a height up to 0.13 R$_\odot$. Therefore, wave turbulence driven by nonlinear interaction between outward propagating waves from the Sun's surface and inward reflected waves may heat a coronal hole plasma enough to sustain 10^6 K temperature in lower corona up to a height of 0.13 R$_\odot$.

Although $\mathcal{R}$ tends to decrease above 0.13 $R_\odot$, reflection may still continue to play a role in heating the plasma at heights up to ≈ 0.5 $R_\odot$. The frequency spectrum of Alfvénic waves measured by Morton et al. (2015) suggest the wave energy is concentrated in frequencies at the lower end of the spectrum. In their measurement, the wave energy peaked at $\sim$ 0.2 mHz, which was the lowest frequency in their dataset. In Fig. 9(b) waves of 0.2 mHz frequency have $\mathcal{R} \geq 10\%$ up to a height of ≈ 0.5 $R_\odot$. The value of $\mathcal{R}$ for wave frequencies above 0.2 mHz progressively decreases from 0.13 $R_\odot$ to ≈ 0.5 $R_\odot$. These two features of Fig. 9(b) suggest that wave reflection from the smooth v_A gradient will play a partial role in heating the plasma via a wave turbulence mechanism but that the the role of reflection is expected to progressively decrease with height from 0.13 $R_\odot$ to ≈ 0.5 $R_\odot$. At heights above ≈ 0.5 $R_\odot$, reflection from the smooth v_A gradient is rather weak and the reflected wave may not be of consequence in heating the plasma.

6. SUMMARY

In this paper, we report the first experimental detection of a reflected Alfvén wave from a strong v_A gradient using a series of experiments in solar-like plasmas. Our results show that a strong v_A gradient is necessary to reflect Alfvén waves, and that the reflected wave energy increases for incident waves having longer wavelengths. The trend in the laboratory wave reflection data agree with the solar observation of Morton et al. (2015), where they showed that the ratio of the outward propagating wave power to the inward propagating wave power increases for longer wavelength waves, i.e., smaller wave frequencies. This indicates that the counter-propagating waves observed by Morton et al. (2015) may be due to wave reflection, supporting their hypothesis.

Two-fluid simulations using the `Gkeyll` code qualitatively agree with and support the experimental detection of a reflected Alfvén wave. In the simulations, we excited Alfvén waves using a model of the ASW antenna. We traced the propagation of Alfvén waves along the plasma column through a uniform B_0 profile, as well as strong and weak v_A gradients. Like the experiments, the simulations show that a strong v_A gradient reflects, while a weak v_A gradient does not. In the future, we will make quantitative comparison after developing a model of an orthogonal ring antenna for simulations similar to the one used in experiment.

We experimentally measured $\mathcal{R}$ for different values of $\lambda_\parallel / L_{A,\min}$ and presented two sets of values of $\mathcal{R}$, i.e., $\mathcal{R}_{z_2}$ and $\mathcal{R}_0$. $\mathcal{R}_{z_2}$ is determined by dividing the measured reflected wave power just after the wave exits from the gradient region by the incident wave power that enters the gradient region. The gradient region is of finite spatial extent, and since simulations showed that wave reflects from the vicinity of the strongest part of the gradient, we estimated the coefficient of reflection near the strongest part, $\mathcal{R}_0$, using $\mathcal{R}_{z_2}$ and a model to take into account collisional damping between the edge of the gradient region and the center of the gradient region. The values of $\mathcal{R}_{z_2}$ and $\mathcal{R}_0$ were found to increase with increasing $\lambda_\parallel / L_{A,\min}$.

A comparison of the laboratory results and solar parameters suggest that Alfvén waves will be reflected by the smooth v_A gradient at heights up to 0.5 $R_\odot$ in coronal holes. Furthermore, solar models suggest that the coefficient of reflection may be sufficient to generate enough inward propagating waves at low heights in a coronal hole ($\lesssim 0.13$ $R_\odot$) to turbulently heat the plasma at these heights. The role of wave reflection from the smooth v_A gradient in heating the plasma is expected to progressively diminish from a height of $\approx$ 0.13 to 0.5 $R_\odot$. In addition, at heights of ≈ 0.5 $R_\odot$ or above, reflection from this gradient may not be adequate to generate enough plasma heating via wave turbulence mechanism requiring other processes like density fluctuation to enhance wave reflection (Shoda et al. 2019; Asgari-Targhi et al. 2021).

APPENDIX

A. PHASE RELATIONSHIP BETWEEN INCIDENT AND REFLECTED WAVE

We performed additional simulations to test the phase relationship between the incident and reflected waves. Profile I was used for the simulations, where the Alfvén wave propagated from a region of low to high velocity. An incident wave having a strong negative b_y was found to produce a reflected wave having a positive b_y, as shown in Fig. 10(a). The direction of propagation of the wave was confirmed by calculating the z component of the Poynting vector, S, given in Fig. 10(b). A positive value of S_z signifies propagation in the $+z$ direction, which is consistent for an incident wave. A reflected wave propagating in the $-z$ direction has a negative S_z value. Therefore, Fig. 10(a) and (b) demonstrates that Alfvén wave reflection from gradient I introduces a 180° phase difference between the incident and reflected wave.

The result of the Alfvén wave reflection simulations agree with the predictions of theory of reflection of light

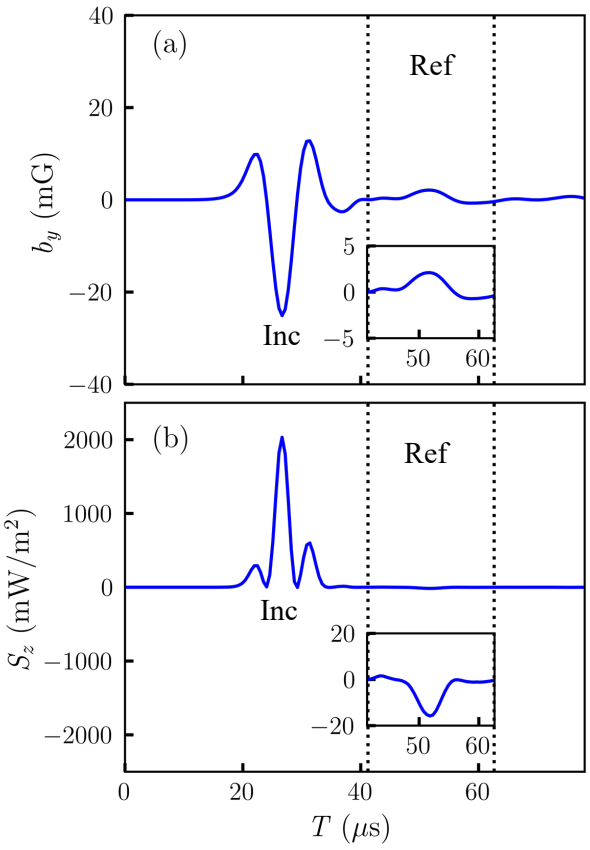

Figure 10. Time variation of (a) b_y and (b) S_z for profile I at $x = y = 0$ and $z = 3.5$ m showing the incident wave referred to as "Inc" and the reflected wave denoted by "Ref".

(Griffiths 2015). According to which, the phase of the magnetic field of a light wave incident on a gradient from the low velocity side is inverted by 180° upon reflection. The reason for the similarity between Alfvén and light waves may be because both are electromagnetic waves.

ACKNOWLEDGEMENTS

This work was supported by US DOE Frontier Plasma Science program and General plasma science program funded by contract number DE- AC0209CH11466. J.M.T. was additionally supported by the NSF CSSI (Cyberinfrastructure for Sustained Scientific Innovation) program, grant number 2209471. D.W.S. and M.H. were supported by the DOE grant DE-SC0021261. J. Juno was supported by the U.S. Department of Energy under Contract No. DE-AC02-09CH1146 via an LDRD grant. The experiments were performed at the Basic Plasma Science Facility (BaPSF), which is a colaborative research facility supported by the DOE and NSF, with major facility instrumentation developed via an NSF award AGS–9724366. The simulations presented in this article were performed on computational resources managed and supported by Princeton Research Computing, a consortium of groups including the Princeton Institute for Computational Science and Engineering (PICSciE) and the Office of Information Technology's High Performance Computing Center and Visualization Laboratory at Princeton University.

DATA AVAILABILITY STATEMENT

The experimental data presented in this paper will be made available upon publication using Princeton's data repository. `Gkeyll` is open source and can be installed by following the instructions on the `Gkeyll` website (http://gkeyll.readthedocs.io). The input and LAPD gradient files for the `Gkeyll` simulations presented here are available in the following GitHub repository, https://github.com/ammarhakim/gkyl-paper-inp.

REFERENCES

Alfvén, H. 1942, Nature, 150, 405, doi: 10.1038/150405d0

Asgari-Targhi, M., Asgari-Targhi, A., Hahn, M., & Savin, D. 2021, The Astrophysical Journal, 911, 63, doi: 10.3847/1538-4357/abe9b4

Bemporad, A., & Abbo, L. 2012, The Astrophysical Journal, 751, 110, doi: 10.1088/0004-637X/751/2/110

Bose, S., Carter, T., Hahn, M., et al. 2019, The Astrophysical Journal, 882, 183, doi: 10.3847/1538-4357/ab2fe0

Bose, S., Fox, W., Ji, H., et al. 2022

Bose, S., Kaur, M., Barada, K. K., et al. 2018, European Journal of Physics, 40, 015803, doi: 10.1088/1361-6404/aaee31

Bose, S., Kaur, M., Chattopadhyay, P., et al. 2017, Journal of Plasma Physics, 83, 615830201, doi: 10.1017/S0022377817000289

Braginskii, S. I. 1965, Review of Plasma Physics, 1, 205

Breun, R., Brooker, P., & Brouchous, D. 1987, in Plasma physics and controlled nuclear fusion research 1986 (International Atomic Energy Agency). https://inis.iaea.org/search/search.aspx?orig_q=RN:18091939

Chandran, B. D., & Hollweg, J. V. 2009, The Astrophysical Journal, 707, 1659, doi: 10.1088/0004-637X/707/2/1659

Churchill, R., & Brown, J. 1987, Fourier Series and Boundary Value Problems, 4th edn. (McGraw-Hill)

Cramer, N. 2011, The Physics of Alfvén Waves (Wiley-VCF)

Cranmer, S. R. 2009, Living Reviews in Solar Physics, 6, 3, doi: 10.12942/lrsp-2009-3

Cranmer, S. R., Asgari-Targhi, M., Miralles, M. P., et al. 2015, Philosophical Transactions of the Royal Society of London Series A, 373, 20140148, doi: 10.1098/rsta.2014.0148

Cranmer, S. R., & Van Ballegooijen, A. 2005, The Astrophysical Journal Supplement Series, 156, 265, doi: 10.1086/426507

Cranmer, S. R., Van Ballegooijen, A. A., & Edgar, R. J. 2007, The Astrophysical Journal Supplement Series, 171, 520, doi: 10.1086/518001

Cross, R. 1988, An Introduction to Alfvén Waves,, Adam Hilger series on plasma physics (Taylor & Francis)

Del Zanna, L., Velli, M., & Londrillo, P. 2001, Astronomy & Astrophysics, 367, 705

Dmitruk, P., Milano, L. J., & Matthaeus, W. H. 2001, The Astrophysical Journal, 548, 482, doi: 10.1086/318685

Drake, D. J., Schroeder, J. W. R., Howes, G. G., et al. 2013, Phys. Plasmas, 20, 072901, doi: 10.1063/1.4813242

Everson, E., Pribyl, P., Constantin, C., et al. 2009, Review of Scientific Instruments, 80, doi: 10.1063/1.3246785

Fludra, A., Del Zanna, G., Alexander, D., & Bromage, B. 1999, Journal of Geophysical Research: Space Physics, 104, 9709, doi: 10.1029/1998JA900033

Gekelman, W., Vincena, S., Leneman, D., & Maggs, J. 1997, Journal of Geophysical Research: Space Physics, 102, 7225, doi: 10.1029/96JA03683

Gekelman, W., Vincena, S., Van Compernolle, B., et al. 2011, Physics of Plasmas, 18, 055501, doi: 10.1063/1.3592210

Gekelman, W., Pribyl, P., Lucky, Z., et al. 2016, Review of Scientific Instruments, 87, 025105, doi: 10.1063/1.4941079

Gigliotti, A., Gekelman, W., Pribyl, P., et al. 2009, Physics of Plasmas, 16, 092106, doi: 10.1063/1.3224030

Goossens, M., Andries, J., Soler, R., et al. 2012, The Astrophysical Journal, 753, 111, doi: 10.1088/0004-637X/753/2/111

Goossens, M., Terradas, J., Andries, J., Arregui, I., & Ballester, J. 2009, Astronomy & Astrophysics, 503, 213, doi: 10.1051/0004-6361/200912399

Griffiths, D. 2015, Introduction to Electrodynamics (Pearson India Education Services Pvt, Ltd.)

Hahn, M., D'Huys, E., & Savin, D. W. 2018, The Astrophysical Journal, 860, 34, doi: 10.3847/1538-4357/aac0f3

Hahn, M., Fu, X., & Savin, D. W. 2022, The Astrophysical Journal, 933, 52, doi: 10.3847/1538-4357/ac7147

Hahn, M., Landi, E., & Savin, D. W. 2012, The Astrophysical Journal, 753, 36, doi: 10.1088/0004-637X/753/1/36

Hahn, M., & Savin, D. W. 2013, The Astrophysical Journal, 776, 78, doi: 10.1088/0004-637X/776/2/78

Hakim, A., Loverich, J., & Shumlak, U. 2006, J. Comp. Phys., 219, 418, doi: 10.1016/j.jcp.2006.03.036

Hara, H. 2019, The Astrophysical Journal, 887, 122, doi: 10.3847/1538-4357/ab50bf

Hershkowitz, N., Auciello, O., & Flamm, D. 1989, Plasma diagnostics, 1, 113

Huba, J., of Naval Research, U. S. O., & (U.S.), N. R. L. 2016, NRL Plasma Formulary, NRL publication (Naval Research Laboratory). https://suli.pppl.gov/2016/course/NRL_FORMULARY_16.pdf

Karavaev, A., Gumerov, N., Papadopoulos, K., et al. 2011, Physics of Plasmas, 18, 032113, doi: 10.1063/1.3562118

Ko, Y.-K., Fisk, L. A., Geiss, J., Gloeckler, G., & Guhathakurta, M. 1997, Solar Physics, 171, 345, doi: 10.1023/A:1004943213433

Landi, E. 2008, The Astrophysical Journal, 685, 1270, doi: 10.1086/591225

Leneman, D. 2007, Physics of Plasmas, 14, 122109, doi: 10.1063/1.2813459

Matthaeus, W. H., Zank, G. P., Oughton, S., Mullan, D. J., & Dmitruk, P. 1999, The Astrophysical Journal Letters, 523, L93, doi: 10.1086/312259

McIntosh, S. W., De Pontieu, B., Carlsson, M., et al. 2011, Nature, 475, 477, doi: 10.1038/nature10235

Mitchell, C., Maggs, J., Vincena, S., & Gekelman, W. 2002, Journal of Geophysical Research: Space Physics, 107, doi: 10.1029/2002JA009277

Moore, R., Suess, S., Musielak, Z., & An, C.-H. 1991a, The Astrophysical Journal, 378, 347, doi: 10.1086/170435

Moore, R. L., Hammer, R., Musielak, Z. E., Suess, S. T., & An, C. H. 1992, ApJL, 397, L55, doi: 10.1086/186543

Moore, R. L., Musielak, Z. E., Suess, S. T., & An, C. H. 1991b, in Mechanisms of Chromospheric and Coronal Heating, ed. P. Ulmschneider, E. R. Priest, & R. Rosner (Berlin, Heidelberg: Springer Berlin Heidelberg), 435–437, doi: 10.1007/978-3-642-87455-0_73

Morton, R., Tomczyk, S., & Pinto, R. 2015, Nature communications, 6, doi: 10.1038/ncomms8813

Musielak, Z., Fontenla, J., & Moore, R. 1992, Physics of Fluids B: Plasma Physics, 4, 13, doi: 10.1063/1.860452

Narain, U., & Ulmschneider, P. 1996, Space Science Reviews, 75, 453, doi: 10.1007/BF00833341

Oughton, S., Matthaeus, W. H., Dmitruk, P., et al. 2001, The Astrophysical Journal, 551, 565, doi: 10.1086/320069

Pedregosa, F., Varoquaux, G., Gramfort, A., et al. 2011, Journal of Machine Learning Research, 12, 2825. http://jmlr.org/papers/v12/pedregosa11a.html

Priest, E. 2014, Magnetohydrodynamics of the Sun (Cambridge University Press), doi: 10.1017/CBO9781139020732

Rasmussen, C. E. 2005, Gaussian processes for machine learning /, Adaptive Computation and Machine Learning series (Cambridge, Mass. :: MIT Press,), doi: 10.7551/mitpress/3206.001.0001

Roberts, D., Hershkowitz, N., Majeski, R., & Edgell, D. 1989, in AIP Conference Proceedings, Vol. 190, AIP, 462–465, doi: 10.1063/1.38448

Shoda, M., Suzuki, T. K., Asgari-Targhi, M., & Yokoyama, T. 2019, The Astrophysical Journal Letters, 880, L2, doi: 10.3847/2041-8213/ab2b45

Stix, T. H., & Palladino, R. 1958, The Physics of Fluids, 1, 446, doi: 10.1063/1.1724362

Swanson, D., Clark, R., Korn, P., Robertson, S., & Wharton, C. 1972, Physical Review Letters, 28, 1015, doi: 10.1103/PhysRevLett.28.1015

Thuecks, D., Kletzing, C., Skiff, F., Bounds, S., & Vincena, S. 2009, Physics of Plasmas, 16, 052110, doi: 10.1063/1.3140037

Van Doorsselaere, T., Nakariakov, V., & Verwichte, E. 2008, The Astrophysical Journal Letters, 676, L73, doi: 10.1086/587029

Vincena, S., Gekelman, W., & Maggs, J. 2001, Physics of Plasmas, 8, 3884, doi: 10.1063/1.1389092

Vincena, S. T. 1999, PhD thesis. https://www.proquest.com/openview/eb25033d38437321d239c07204214858/1?pq-origsite=gscholar&cbl=18750&diss=y

Vranjes, J., Petrovic, D., Poedts, S., Kono, M., & Čadež, V. 2006, Planetary and Space Science, 54, 641, doi: 10.1016/j.pss.2005.12.015

Wang, L., Hakim, A. H., Bhattacharjee, A., & Germaschewski, K. 2015, Phys. Plasmas, 22, 012108, doi: 10.1063/1.4906063

Wang, L., Hakim, A. H., Ng, J., Dong, C., & Germaschewski, K. 2020, J. Comp. Phys., 415, 109510, doi: 10.1016/j.jcp.2020.109510

Yasaka, Y., Majeski, R., Browning, J., Hershkowitz, N., & Roberts, D. 1988, Nuclear Fusion, 28, 1765, doi: 10.1088/0029-5515/28/10/005

Zhang, Y., Heidbrink, W., Boehmer, H., et al. 2008, Physics of Plasmas, 15, 012103, doi: 10.1063/1.2827518